pubs.acs.org/Biomac

Article

Intrinsic Fluorescence in Peptide Amphiphile Micelles with Protein-Inspired Phosphate Sensing

Whitney C. Fowler*

Cite This: *Biomacromolecules* 2022, 23, 4804−4813

Read Online

ACCESS | Metrics & More | Article Recommendations | Supporting Information

ABSTRACT: Although peptide amphiphile micelles (PAMs) have been widely studied since they were developed in the late 1990s, to the author's knowledge, there have been no reports that PAMs intrinsically fluoresce without a fluorescent tag, according to the aggregation-induced emission (AIE) effect. This unexpected fluorescence behavior adds noteworthy value to both the peptide amphiphile and AIE communities. For PAMs, intrinsic fluorescence becomes another highly useful feature to add to this well-studied material platform that features precise synthetic control, tunable self-assembly, and straightforward functionalization, with clear potential applications in bioinspired materials for bioimaging and fluorescent sensing. For AIE, it is extremely rare and highly desirable for one platform to exhibit precise tunability on multiple length scales in aqueous solutions, positioning PAMs as uniquely well-suited for systematic AIE mechanistic study and sequence-specific functionalization for bioinspired AIE applications. In this work, the author proposes that AIE occurs across intermolecular emissive pathways created by the closely packed peptide amide bonds in the micelle corona upon self-assembly, with maximum excitation and emission wavelengths of 355 and 430 nm, respectively. Of the three PAMs evaluated here, the PAM with tightly packed random coil peptide conformation and maximum peptide length had the largest quantum yield, indicating that tuning molecular design can further optimize the intrinsic emissive properties of PAMs. To probe the sensing capabilities of AIE PAMs, a PAM was designed to incorporate a protein-derived phosphate-binding sequence. It detected phosphate down to 1 ppm through AIE-enhanced second-order aggregation, demonstrating that AIE in PAMs leverages tunable biomimicry to perform protein-inspired sensing.

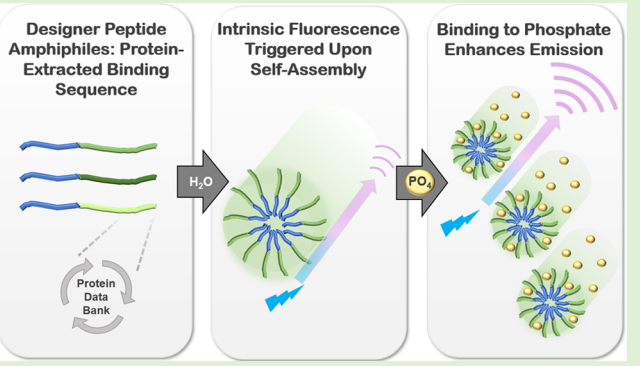

1. INTRODUCTION

Engineering functional biomimetic materials has become a rich field of study that harnesses insights from evolutionarily optimized biological materials and translates these findings to synthetic materials. One quintessential biomimetic material is peptide amphiphile micelles (PAMs).[1−4] Peptide amphiphiles (PAs) consist of a peptide headgroup conjugated to a hydrophobic tail that spontaneously self-assembles into micelles in water to display the peptide to the aqueous environment. PAMs fuse strategic material design and fundamental study with a diverse and creative array of applications including targeted drug delivery,[5] protein purification,[6] nutrient reclamation,[7] nerve regeneration,[8] and tissue scaffolding for spinal cord recovery.[9] This wide breadth of functionality is directly linked to tunable material design advantages. The precisely controlled synthesis yields a monodisperse product for sequence-specific biomimetic applications. The PA-to-PA interactions within the micelle can be tuned to control the self-assembled architecture and conformational secondary structure.[10−13] Multicomponent composite materials can be easily fabricated to engineer in advanced multifaceted use in one material platform.[14,15]

Interestingly, despite the thorough study and diverse use of PAMs over the past two decades, to the author's knowledge, no one has reported that this class of materials possesses unexpected fluorescence behavior without a fluorescent tag. This exciting discovery adds an additional desirable feature to this already robust material platform that pairs well with many current uses of PAMs, such as bioimaging and sensing.

Recent reports of other unexpectedly fluorescent materials led to this discovery.[16,17] These intriguing systems similarly did not contain aromatic rings to suggest fluorescence *a priori*; instead, they featured electron-rich moieties in lone pairs of oxygens[18−20] or the double bond of an amide.[21] Nevertheless, these materials possessed two parameters required to exhibit fluorescence through a phenomenon known as aggregation-

Received: August 2, 2022
Revised: September 30, 2022
Published: October 12, 2022

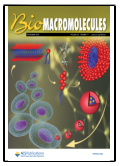

https://doi.org/10.1021/acs.biomac.2c00960
Biomacromolecules 2022, 23, 4804−4813

induced emission (AIE): that (1) electron-rich moieties be "space conjugated," rather than covalently conjugated, to be close enough to create emission pathways between subfluorophoric molecules, and (2) these moieties be restricted in vibrational or rotational motion to minimize energy loss through those modes. Liu et al. reported unexpected fluorescence for a material with remarkably similar features to PAMs, namely, surfactant micelles with closely packed amide bonds at the hydrophobic/hydrophilic corona interface.[21] Since PAMs likewise possess closely packed amide bonds in the micelle corona, they were evaluated at identical excitation and emission conditions, which unveiled their undiscovered intrinsic fluorescence behavior.

While AIE has yet to be reported for PAMs, there have been reports of AIE of bioinspired materials as far back as 2001,[22,23] coinciding with the discovery of AIE itself. AIE was first reported by Tang, et al. for 1-methyl-1,2,3,4,5-pentaphenylsilole that by itself was weakly emissive but upon aggregation exhibited a sharp increase in fluorescence,[24] sparking many aromatic AIE materials to be designed and characterized. That same year, Swaminathan et al. reported fluorescence of a highly concentrated L-lysine solution, a feature that was attributed to AIE.[22] Both amyloidlike fibers[25] and self-assembled oligosaccharides[26] have been found to fluoresce, prompting numerous studies to understand and optimize biological or biomimetic AIE materials,[27−29] with exciting developments in sensing applications.[30−33] However, AIE materials have historically possessed several distinct disadvantages to overcome to be practically viable, including poor solubility in water due to aromatic components, a lack of hierarchical self-assembling control,[34] complicated synthetic routes, and challenge in functionalization for application.[28] Peptide amphiphile micelles inherently overcome all of these limitations in one highly tunable platform.

In this work, the author presents fundamental characterization of this newly discovered intrinsic fluorescence in peptide amphiphile micelles and highlights their promise as a bioinspired sensing platform with phosphate detection. Overall, this discovery of AIE in a well-studied, highly tunable, widely applicable, and easily functionalized material unveils a controllable approach for systematic study of the mechanism of AIE and a strategic platform for rationally designed protein-inspired sensing applications.

2. EXPERIMENTAL METHODS

2.1. Synthesis and Purification of Peptide Amphiphile Micelles and Micelle Preparation Procedure. Three peptide sequences (GGGGGK, GGGGGSGAGKT, and SSSSSSGAGKT) were synthesized on 0.25 mmoles of rink amide resin (Novabiochem) through standard FMOC solid-phase peptide synthesis using an automated Prelude X Benchtop Synthesizer (Protein Technologies, Tuscon, AZ). For each coupling step, the FMOC protecting group was first removed from the resin using 20% piperidine in dimethylformamide (DMF). Separately, the amino acid (AA) was activated with *N*,*N*,*N*′,*N*′-tetramethyl-*O*-(1*H*-benzotriazol-1-yl)uranium hexafluorophosphate (HBTU) and *N*,*N*-diisopropylethylamine (DIPEA) in a molar ratio of 1:4:3.95:8 of resin/amino acid/HATU/DIPEA. The activated amino acid cocktail was then added to the deprotected resin and then allowed to mix to conjugate. After the amino acid couplings were completed, the deprotected glycine N-terminus was then coupled with a palmitic acid tail.

After drying the resin under nitrogen, the peptide amphiphiles were then cleaved from the resin using a ratio of 95:2.5:2.5 by volume of trifluoroacetic acid: triisopropylsilane: Milli-Q water cleavage cocktail for 2 h while shaking. The cleaved peptide amphiphiles were then precipitated through dropwise addition of the cleavage solution in a ratio of 50:50 by volume of hexanes: −80 °C diethyl ether solution. The peptide amphiphiles were dried under nitrogen and dissolved in water.

The peptide amphiphiles were purified using reverse-phase high-performance liquid chromatography (HPLC) (Prominence, Shimadzu, Columbia, MD) on a C8 column (Waters, Milford, MA) at 50 °C using acetonitrile and water with 0.1% formic acid as gradient mobile phases. The molecular weights of the products in the HPLC fractions were characterized by matrix-assisted laser desorption/ionization time-of-flight (MALDI-TOF) mass spectral analysis (Biflex III, Bruker, Billerica, MA). The product-verified fractions were lyophilized and stored as powders at −20 °C. The purity was analyzed using a similar gradient method on an Agilent 6130 LC-MS system in the University of Chicago's Mass Spectrometry Facility, using a Waters column, C8, XBridge, 4.6 mm × 150 mm, 5 μm particle size, and 130 Å pore size. The purity was calculated by integrating the area under the peaks during the elution time and dividing the area of the product peak by the area of all peaks, excluding peaks that were artifacts of the method. The purity was confirmed to be greater than 95% for all PAs. The precise PA concentration for the purified samples was calculated by amino acid analysis (AAA), which was performed by the Molecular Structure Facility at the University of California Davis. The PA samples were then lyophilized in fractions for storage until later use. To fabricate the micelles, the lyophilized PAs were dissolved in Milli-Q water at the desired concentration, heated at 70 °C for 1 h on a mechanical shaker, and equilibrated to room temperature before experimental use.

2.2. Negative-Stain Transmission Electron Microscopy (TEM) Imaging. Carbon film 200 mesh copper grids were glow discharged with a Gatan Solarus plasma cleaning system for 30 s. They were then loaded with 3.5 μL of PAs for 1 min and then the excess was removed through blotting with a filter paper. The grids were negatively stained with 0.75% uranyl formate for 45 s, blotted off to remove excess stain, and then were allowed to air-dry before imaging. All TEM imaging was performed with a Technai G2 F30 (FEI) electron microscope operating at 300 kV. The images were processed digitally using ImageJ software. For the PA samples with phosphate, before sample incubation and staining, equal volumes (2 μL) of sample and PO_4 were mixed on parafilm for 1 min. After 1 min, all 4 μL were transferred onto the grid and stained as previously described.

2.3. Confocal Fluorescence Microscopy Imaging. The PA samples were loaded on a transparent microscope slide and imaged with a Leica Stellaris 8 FALCON (Buffalo Grove, IL) on a DMI-8 stand and a 63×/1.40 oil objective. The white light laser was set to 460 nm with reflection mode to the HyD detector and pinhole of 0.2 Airy units. The scan rate was 2 kHz, and line average was 48. The reflection method used was based on a previously published method.[35] Fluorescence images were taken with 405 nm laser illumination. The images were processed using ImageJ.

2.4. UV−Vis Absorbance Measurements. The measurements were recorded using a Shimadzu UV-3600 Plus UV−vis−NIR spectrophotometer (Columbia, MD). The samples were transferred to a quartz crystal cuvette with a 10 mm pathlength, and the absorbance was scanned from 200 to 800 nm for PA samples at concentrations of 100, 250, 500, and 1000 μM and quinine sulfate in 0.1 M H_2SO_4 at concentrations of 1, 5, and 7 μg/mL.

2.5. Excitation and Emission Scan Measurements Using Fluorescence Spectrometry. The measurements were recorded using a Horiba Fluorolog-3 (Irvine, CA) equipped with a dual monochromator to minimize light scattering from the micelles, which produces additional noise. For the pure PA experiments, a quartz crystal cuvette with a 10 mm pathlength was loaded with the PA sample and transferred to the instrument. The excitation scans were recorded for PA samples of 11 mM at an emission wavelength of 430 nm and excitation values ranging from 200 to 405 nm with an excitation slit width of 5 nm and an emission slit width of 14 nm. The emission scans for Figures 3B, S7B, and S8B were recorded for PA samples of 11 mM at an excitation wavelength of 355 nm and emission values ranging from 370 to 650 nm, with an excitation slit width of 3 nm and an emission slit width of 10 nm. The emission scans for Figures 3C, S7C, and S8C were recorded for PA samples at concentrations of 100, 250, 500, and 1000

https://doi.org/10.1021/acs.biomac.2c00960
Biomacromolecules 2022, 23, 4804−4813

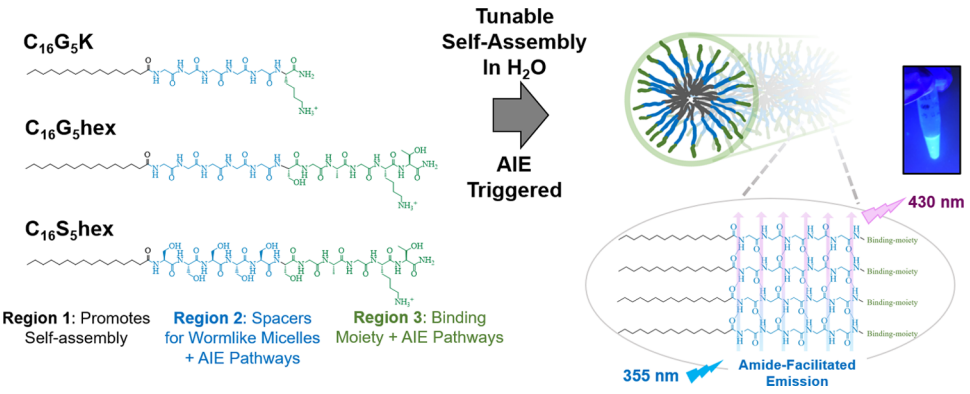

Figure 1. Molecular structures of $C_{16}G_5K$, $C_{16}G_5hex$, and $C_{16}S_5hex$ with three building block regions to control (1) self-assembly, (2) wormlike micelle formation, and (3) bioinspired binding function, with both peptide regions contributing to AIE (left). The PA molecules spontaneously self-assemble in water, yielding intrinsically emissive PA micelles that fluoresce due to tightly backed peptide amides in the micelle corona. The photo (right) depicts bulk solution fluorescence of $C_{16}G_5hex$.

μM at an excitation wavelength of 355 nm and emission values ranging from 370 to 650 nm, with an excitation slit width of 5 nm and an emission slit width of 14 nm. The emission scans of quinine sulfate were recorded at concentrations of 1, 5, and 7 μg/mL at identical conditions. For the PA plus phosphate experiments, phosphate was added to a PA solution in a 1.5 mL centrifuge tube to achieve a final concentration of 1000 μM $C_{16}G_5hex$ and final phosphate concentrations ranging from 10 to 1000 μM. The solutions were centrifuged using a benchtop 1.5 mL centrifuge at high speed for 5 min. The supernatant was collected and transferred to the 10 mm pathlength quartz crystal cuvette. The emission scans were performed as described.

2.6. Critical Micelle Concentration (CMC) Determination Using DPH Dye. The true CMC was calculated by marking an increase of fluorescence intensity, corresponding to an increased micelle concentration, of a dissolved dye that fluoresces in the presence of hydrophobic micelle cores. To execute this experiment, 1,6-diphenyl-1,3,5-hexatriene (DPH) dye was dissolved in tetrahydrofuran at a concentration of 100 mM and then diluted in water to a final concentration of 1 μM. Each PA was dissolved in 1 μM DPH solution and serially diluted by half to range from 0.05 to 500 μM, performed in triplicates for each PA. The dilutions were allowed to equilibrate for 1 h while being covered with aluminum foil at room temperature and then were transferred to a 384-well plate. Their fluorescence intensity was measured using a Tecan Infinite 200 plate reader (Mannedorf, Switzerland) with an excitation wavelength of 360 nm and an emission wavelength of 430 nm. The data were plotted with a log-transformed concentration. The CMC was identified as the concentration at which the fluorescence value is greater than that of 20% above the zero-slope baseline region.

2.7. Fluorescence Critical Micelle Concentration (FCMC) Determination. The fluorescence critical micelle concentration was calculated simply by serially diluting the PA stock concentration by half to range from 2 to 4000 μM. The dilutions were transferred to a 384-well plate. The fluorescence intensity was measured and calculated as for the CMC calculations, but with an excitation wavelength of 355 nm. When plotted with the CMC data, the FCMC data were shifted down by 1500 au and scaled by 10 to emphasize the inflection point comparison.

2.8. Circular Dichroism (CD) Spectroscopy Measurements. A quartz crystal cuvette with a 0.1 cm pathlength was loaded with 200 μL of PA samples at 100 μM. Samples were measured at room temperature using a Jasco J-815 Circular Dichroism Spectropolarimeter (Easton, MD). Three scans were performed for each sample from 190 to 250 nm with 0.1 nm step size, and the data were averaged between scans. The data were converted to mean residue ellipticity and fit according to a minimum-energy calculation of a linear combination of α helix, β sheet, and random coil models.

2.9. Gel Fluorescence Imaging. The samples were prepared by depositing 16 μL of 5 mM $C_{16}G_5hex$ onto a nonfluorescent black plate and then adding 4 μL of a given combination of Milli-Q water and 20 mM Na_2HPO_4 stock to achieve final concentrations of 4 mM $C_{16}G_5hex$ and 0, 1, 2, and 4 mM PO_4. When phosphate was added to the PA droplet, the droplet was gently stirred with the tip of the pipette to ensure complexation of the PA with phosphate. The samples were prepared in triplicate. The plate was transferred to a BioRad ChemiDoc MP Molecular Imager (Hercules, CA), and fluorescence images were taken using a 530/28 emission filter and an exposure time of 10 s. The integrated fluorescence density of each sample droplet was calculated using ImageJ imaging software.

2.10. Phosphate-Binding Experiments. Samples were prepared in Milli-Q water in molar ratios of 1:1:1:1, 2:1:1:1, and 4:1:1:1 of PA/PO_4/NO_3/NO_2, equivalent to 10 ppm PO_4. The salts used were Na_2HPO_4, $NaNO_3$, and $NaNO_2$. The pH was adjusted to the desired pH condition using minimal HCl and NaOH, and the pH was measured using a Fisher Scientific Accumet XL500 pH/ISE/Conductivity Benchtop Meter (Vernon Hills, IL) and a Fisherbrand Accumet Micro Glass Mercury-Free Combination Electrode. Upon reaching the target pH, the solution was filtered using a 13 mm 0.22 μm GHP Acrodisc syringe filter to separate the unbound anions from the PA-anion bound complexes. The filtrate was analyzed using ion chromatography using a Thermo Scientific Dionex ICS-5000+ equipped with a Dionex AS-DV autosampler and using a Dionex IonPac AS22 column (Product No. 064141, Thermo Scientific, California). The analysis was run using an eluent of 4.5 mM sodium carbonate and 1.4 mM sodium bicarbonate (Product No. 063965 from Thermo Scientific, California) and a Dionex AERS 500 Carbonate 4 mm Electrolytically Regenerated Suppressor (Product No. 085029 from Thermo Scientific, California). The experiments were performed in duplicate for each condition.

2.11. Safety Comment. No unexpected or unusually high safety hazards were encountered during these experiments.

3. RESULTS AND DISCUSSION

3.1. Design of Peptide Amphiphile Materials for AIE Insight. PAMs have boasted of facile incorporation of sequence-specific regions to precisely control biomimetic function.[36,37] Here, three PA molecules were designed with three building block regions each (Figure 1). Region 1 promotes hydrophobic self-assembly. Region 2 consists of closely packed amino acid (AA) residues shown to dictate micelle architecture[37] and secondary structure[12] through their interchain interactions, thus likely also strongly impacting AIE function. Region 3 is a protein-extracted binding moiety. The goals of the PA design were 2-fold: (1) to directly compare the impact of the tightly packed Region 2 on AIE performance, and (2) to determine the impact of incorporating a functional binding sequence (Region 3) on AIE performance to probe the potential

https://doi.org/10.1021/acs.biomac.2c00960
Biomacromolecules 2022, 23, 4804−4813

for designing dual-function PAMs with AIE and bioinspired sensing.

The design regions of the three PAs $C_{16}G_5K$, $C_{16}G_5$hex, and $C_{16}S_5$hex are derived from a recently engineered PAM that selectively sequesters phosphate, denoted as $C_{16}G_3$hex,[7] to evaluate the new AIE property on a well-characterized and functionally useful molecular system. Region 1 of $C_{16}G_3$hex was a 16-carbon hydrophobic tail, conserved in all three PAs here and denoted with C_{16} in the nomenclature. Its Region 2 consisted of three glycine spacers that were selected to promote self-assembly into wormlike micelles due to tight packing and interchain hydrogen-bonding. The number of spacer residues was increased from three to five in the three PAs in this study to amplify this region's potential intermolecular AIE effect, since residues closer to the micelle core are packed more tightly than AA residues that extend further into the aqueous environment. Region 3 of $C_{16}G_3$hex was a hexapeptide phosphate-binding moiety that was extracted from a class of phosphate-binding proteins in the protein data bank.[38] It also likely contributes to AIE. This hexapeptide sequence, denoted with "hex" in the nomenclature, was conserved in both $C_{16}G_5$hex and $C_{16}S_5$hex.

$C_{16}G_5$hex was designed to nearly identically match $C_{16}G_3$hex, and then two variations were derived to address each of the above aims. In the first pair, $C_{16}G_5$hex was directly compared to $C_{16}G_5K$ to determine the impact of incorporating a protein-derived binding sequence on AIE. They have identical Regions 1 and 2, but the hexapeptide binding sequence of $C_{16}G_5$hex was replaced with a single lysine residue in $C_{16}G_5K$, which was required for solubility. The second pair, $C_{16}G_5$hex and $C_{16}S_5$hex, was designed to probe the impact of Region 2 on AIE. Regions 1 and 3 are identical, but the glycine residues of $C_{16}G_5$hex were replaced with serine residues in $C_{16}S_5$hex. Glycine residues in Region 2 have been reported to promote wormlike micelle formation in PAMs due to being able to pack tightly,[39] which could amplify AIE. Alternatively, the hydroxyls of the serine residues could also contribute to AIE. Gong et al.[19] and Niu et al.[20] observed unexpected AIE in materials with hydroxyl groups and no pi orbitals, Gong et al. reported an emission peak and shoulder of 382 and 433 nm when excited at 365 nm, and Niu et al. observed an emission peak of 430 nm when excited at 360 nm. Both results are similar to the reported amide excitation and emission wavelengths. Additionally, Region 2 of PAs has been determined to strongly impact the secondary structure that peptides adopt within the headgroup,[12,13] a factor that has also been reported to affect AIE.[40,41] For all sequences, typical fluorescent AA residues such as tryptophan were intentionally omitted to study the unexpected fluorescence from nonaromatic PAs.

Each of these molecules was synthesized using solid-phase peptide synthesis, a technique that enables precise synthetic control through stepwise amino acid coupling. Precise control is essential to incorporating these functional building block regions and is a noteworthy advantage of PAMs.

3.2. Self-Assembly Verification through Imaging. PAMs not only possess synthetic tunability but also can be designed to self-assemble into a predictable range of micellar constructs by controlling two properties: (i) the packing parameter for surfactant molecules[42,43] and (ii) the interpeptide interactions, particularly in Region 2 of the molecular design. The packing parameter, P, relates the chemistry of the molecule to its packed self-assembled state in the micelle using the ratio $P = v/al$, where v and l are the volume and maximum extended length of the tail, respectively, and a is the area of the headgroup at the interface. These molecular design variables can be tuned to achieve different ratios that correlate to the given self-assembled architectures, such as $P < 1/3$ corresponding to spherical micelles and $1/3 < P < 1/2$ corresponding to wormlike micelles. Second, the design of interpeptide interactions also strongly impacts the self-assembled architecture. Densely packable glycine, alanine, and valine residues have been shown to promote wormlike micelle formation,[37] while charged residues such as lysine or glutamic acid have been shown to repulsively interact and drive self-assembly into spherical micelles.[7,44] This aggregation control further elevates PAMs as a desirable platform to systematically elucidate mechanistic insight of AIE related to aggregate properties.

In this study, the interactions of Region 2 were designed to yield consistent micellar architecture to enable direct comparison of AIE features between systems. It was also hypothesized that wormlike micelles may be more emissive than spherical micelles since the PA molecules are more closely packed. Hence, glycine and serine residues were chosen for the Region 2 residues, which both interact with nearby chains in a packed state and would be likely to yield wormlike micelles upon self-assembly.

The self-assembly properties of the systems were visualized using both negative-stain transmission electron microscopy (TEM) and confocal fluorescence microscopy (Figure 2). The TEM images indicated that the PAMs all self-assemble into wormlike micelles that extend microns in length, yielding the desired consistency between systems. The reflective imaging technique used for confocal microscopy uniquely captures the fluorescence properties of the individual PAMs.[35] The images

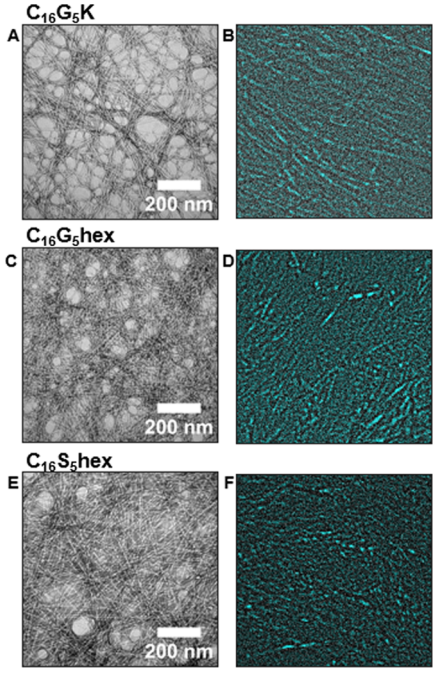

Figure 2. Negative-stain TEM images (left) and confocal fluorescence microscopy images (right) of $C_{16}G_5K$, $C_{16}G_5$hex, and $C_{16}S_5$hex. Both visualize self-assembly into wormlike micelles. The fluorescence microscopy images depict cross-sectional snapshots of fluorescent wormlike micelles that are suspended in a bulk fluorescent droplet of AIE PAMs. The scale bar for the confocal images is omitted because the imaging technique used magnifies the constructs beyond true scales. The reader is instead referred to the TEM images for correct scaling.

https://doi.org/10.1021/acs.biomac.2c00960
Biomacromolecules 2022, 23, 4804−4813

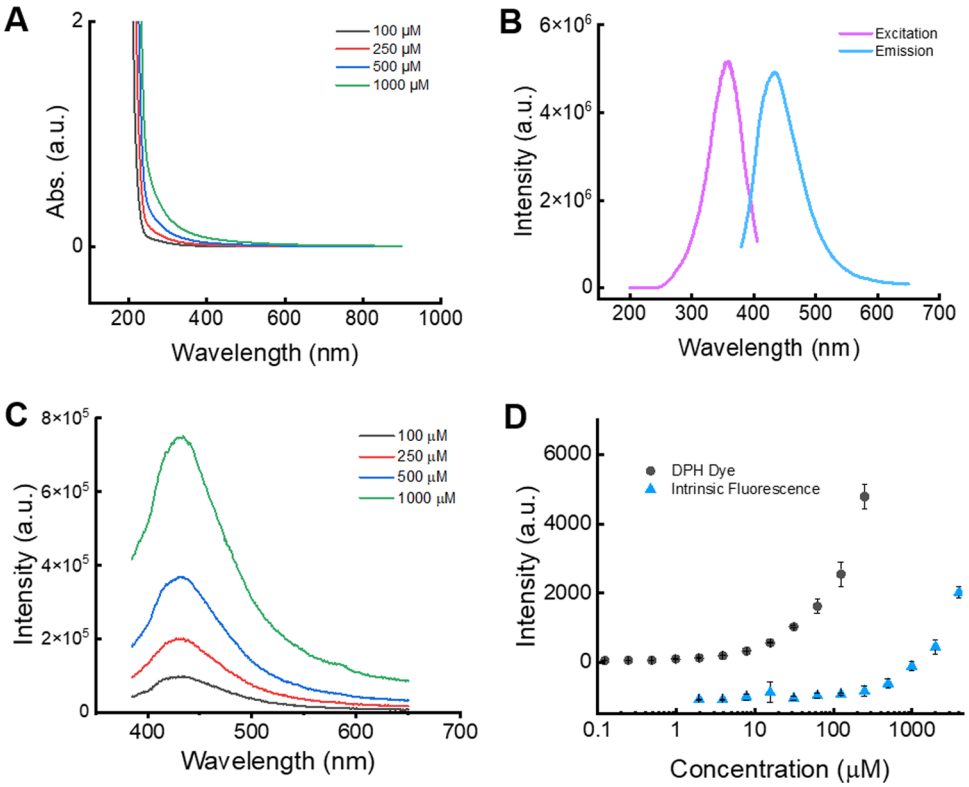

Figure 3. Fundamental fluorescence characterization data for $C_{16}G_5$hex, including (A) absorbance intensity, (B) excitation scan at 430 nm emission and emission scan at 355 nm excitation, (C) fluorescence emission intensity at an excitation of 355 nm, and (D) critical micelle concentration (CMC) using 1,6-diphenyl-1,3,5-hexatriene (DPH) dye and the intrinsic fluorescence critical micelle concentration (FCMC). Note: the FCMC data are offset by 1500 au and scaled by 10 for visualization purposes to avoid overlap of datapoints and to emphasize the inflection point shift.

visualize cross-sectional snapshots of fluorescent PAM micelles suspended in a bulk fluorescent droplet of AIE PAMs, which appears as a fluorescent background in the images. The imaging technique was also able to construct a three-dimensional (3D) rendering of the micelles in the droplet (see Supporting Information, Video S1), which allows one to reconstruct how the extended micelles are arranged in their native liquid state. Overall, while these wormlike micelle systems constitute a consistent preliminary study between like systems, the aggregation properties of this platform can be readily tuned in future studies to directly probe how the self-assembled architecture impacts AIE properties in PAMs.

3.3. Fundamental AIE Properties in PAMs. After visualizing individual micelle fluorescence, the bulk fundamental fluorescence features were characterized for all three systems. Figure 3 depicts the results for $C_{16}G_5$hex. The reader is referred to Figures S7 and S8 for data for $C_{16}G_5K$ and $C_{16}S_5$hex, respectively, which exhibit nearly identical trends for these fundamental experiments. Experiments were performed at room temperature and in Milli-Q water. All three systems possess a shoulder in the absorbance spectra (Figure 3A), blue-shifted after the characteristic 220 nm absorbance peak for peptides. The maximum excitation and emission occur at 355 and 430 nm, respectively (Figure 3B). The fluorescence emission intensity increased as the concentration is increased from 100 to 1000 μM (Figure 3C). There were no peak shifts or additional shoulders as the concentration increased, indicating the fluorescence enhancement is likely due to the concentration rather than a shift in the AIE mechanism. All of these results are consistent with a previous work that reported AIE of molecules with amide bonds.[21] This suggests a similar proposed emission mechanism, namely, that emission occurs across stabilized amide bonds in close proximity within the peptide corona of the micelle.

To investigate the aggregation conditions required for AIE, the true critical micelle concentration (CMC) of the micelles, which is the concentration at which PA molecules begin to self-assemble, was compared to the fluorescence critical micelle concentration (FCMC), the concentration at which AIE begins to occur (Figure 3D). The true CMC was determined using 1,6-diphenyl-1,3,5-hexatriene (DPH) dye, a standard procedure for calculating CMCs for surfactant molecules.[45] Serial dilutions of PAs were dissolved in an aqueous solution with a DPH dye, which fluoresces only when the dye partitions into hydrophobic cores. Thus, an increase in fluorescence indicates that hydrophobic-core micelles are beginning to form, yielding the CMC. The intrinsic fluorescence data was measured without any added dye at an excitation wavelength of 355 nm and an emission wavelength of 430 nm. Both the CMC and the FCMC values were calculated as the concentration value at which the fluorescence intensity value was greater than 20% above the baseline value.

The true CMCs were calculated to be 2, 1, and 1 μM for $C_{16}G_5K$, $C_{16}G_5$hex, and $C_{16}S_5$hex, respectively. The FCMC for all systems was reported as 60 μM, though there is possibly minor variation between systems beyond one significant digit that was not captured in the concentrations measured. This order of magnitude increase indicates that a critical number of PA unimers must be present and closely packed enough to demonstrate AIE. It is also assumed that the PAMs near the CMC more closely resemble spherical micelles or short rods compared to the extended wormlike micelles visualized in Figure 2, which are well above the CMC. It seems feasible that extended

https://doi.org/10.1021/acs.biomac.2c00960
Biomacromolecules 2022, 23, 4804−4813

wormlike micelles could be more emissive than smaller aggregates, as they provide a less interrupted emission pathway and more closely packed components. Future studies are required to determine the precise impact of micelle architecture on the PAM AIE effect.

It is worth noting that the DPH dye excitation and emission wavelengths are 360 and 430 nm, respectively, nearly identical to the PA system. In this case, the fluorescence intensity increase is offset enough to not interfere with the CMC calculation at low concentrations, but this might not always be the case for other PA systems. Interference seems inevitable at concentrations equal to and higher than the FCMC. For future DPH CMC experiments, this interference could be minimized by increasing the DPH concentration several-fold to nullify the less emissive AIE effect at higher concentrations.

The quantum yields (QYs) of these PAMs were calculated to normalize and compare the emissive properties between PAM systems, which revealed the first major discrepancy. The QYs were determined by comparing linear fluorescence intensity vs. absorbance curves to a standard solution of quinine sulfate in 0.1 M H_2SO_4 solution (Figure S9).[46,47] $C_{16}G_5$hex had the highest QY at 1.30%, while $C_{16}G_5K$ and $C_{16}S_5$hex had QYs of 0.85 and 0.82%, respectively. To understand the nearly doubled QY for $C_{16}G_5$hex compared to the other systems, the intermolecular interactions were probed using circular dichroism (CD) spectroscopy (Figure 4). The CD spectra revealed a

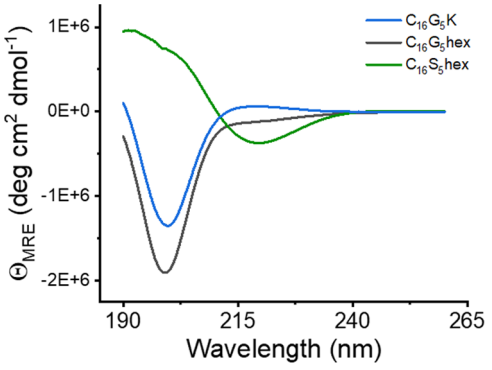

Figure 4. Circular dichroism spectra for $C_{16}G_5K$, $C_{16}G_5$hex, and $C_{16}S_5$hex. $C_{16}G_5K$ and $C_{16}G_5$hex display characteristic properties of a random coil configuration with no secondary structure or ordering. $C_{16}S_5$hex largely adopts an ordered β-sheet structure within the peptide headgroup.

predominantly random coil arrangement of peptide chains within the micelle corona for $C_{16}G_5K$ and $C_{16}G_5$hex, indicated by the characteristic minima near 200 nm. On the other hand, the spectra for $C_{16}S_5$hex indicated that β-sheet hydrogen-bonding occurred between peptides in the corona, with a negative band near 220 nm and a maximum near 190 nm. This is likely facilitated through the hydrogen-bonding hydroxyl groups of the serine residues.

To understand the QY difference, the CD conformational data is paired with molecular design insight as we consider the two PAM pairs separately. The second pair, $C_{16}G_5$hex and $C_{16}S_5$hex, has otherwise identical peptide designs apart from Region 2 spacer residues. The exchange of glycine to serine residues in this region had a noteworthy effect on the secondary structure, shifting the interpeptide interactions from disordered to ordered hydrogen-bonded β-sheets. Several previous studies have probed the effect of the secondary structure on AIE,[40,41] and Lin et al. found that the random coil conformation facilitated the largest AIE properties compared to both α helices and β sheets.[40] The lack of structure enabled the peptide chains to pack more tightly, leading to the not necessarily intuitive conclusion that close proximity of subfluorophores is more important in enhancing emission than adopting ordered emission pathways through β-sheet hydrogen-bonding. This work's results align well with previous findings. The QY difference between the glycine and serine systems also supports the conclusion that the excess lone electron pairs of the hydroxyl groups do not translate to a higher QY for $C_{16}S_5$hex even though other systems relied exclusively on this functional group to achieve AIE.[18,19] Either the hydroxyl groups are not densely packed enough to significantly contribute to AIE in the micelle compared to solid oxygen-based AIE materials like fluorescent rice and starches[19] or the AIE due to the amide bonds is a much greater contributor in this system.

The QY discrepancy between the first pair, $C_{16}G_5$hex and $C_{16}G_5K$, can be understood by considering molecular design differences since they both exhibit random coil conformation. $C_{16}G_5K$ has five fewer AA residues than $C_{16}G_5$hex and is otherwise identical. This confirms that the emissive pathways for AIE are not just limited to Region 2 but also occur across the amide bonds of Region 3 as well, suggesting that further increasing peptide building block length would enhance AIE intensity in future iterations of design. Overall, these findings highlight the direct effect of molecular engineering on AIE performance, indicating the significant potential to optimize the QY of PAMs.

3.4. PAM Design Utilizing Second-Order Aggregation AIE to Sense Phosphate. Peptide amphiphile micelles have also been referred to as "protein analogous micelles,"[48] a name that encompasses their unique biomimicking functionality. Here, the phosphate-binding ability of $C_{16}G_5$hex is combined with this newly discovered AIE to engineer a new sensing platform that leverages the targeted molecular-recognition ability of proteins.

$C_{16}G_3$hex, the predecessor to $C_{16}G_5$hex, was originally engineered to be a capture-and-recovery platform to sequester phosphate for reuse from agricultural runoff.[7] This runoff is often rich in excess fertilizer, which causes severe eutrophication in downstream bodies of water.[49] Concurrently, the global supply of phosphate is being rapidly depleted, prompting calls for creative methods to reclaim and conserve it.[50,51] There has also been complementary interest in designing phosphate-specific sensors to detect phosphate concentration in soil in real-time.[52] This data would be highly valuable to farmers who could adjust their fertilizer distribution accordingly, preventing large fertilizer excesses from entering the runoff and damaging local ecosystems. Phosphate-binding PAMs are well-positioned to be evaluated as phosphate sensors to this end.

$C_{16}G_5$hex was selected for sensing evaluation since it had the highest emissive properties of the three PAMs, likely increasing its sensitivity. The selective binding ability of $C_{16}G_5$hex was evaluated over nitrate and nitrite, the key competing ions in agricultural runoff. $C_{16}G_5$hex was confirmed to bind to phosphate selectively over nitrate and nitrite in a similar fashion as the prototype $C_{16}G_3$hex material (Figure S13). At a 4:1:1:1 molar ratio of PA to each anion, 96% of phosphate was bound, while nitrate and nitrite were only bound at 27 and 17%. As the ratio of PA decreases to equimolar, the amount of nitrate and nitrite bound decreased to 8 and 9%, respectively, while 32% of phosphate was bound. While a high PA/PO_4 ratio is needed to

https://doi.org/10.1021/acs.biomac.2c00960
Biomacromolecules 2022, 23, 4804−4813

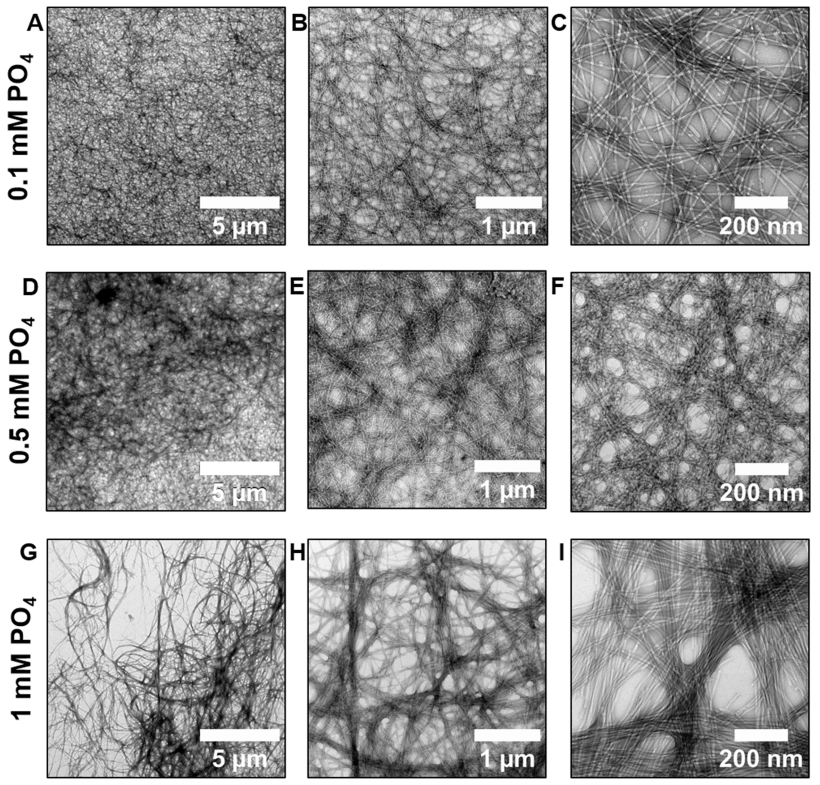

Figure 5. TEM images of $C_{16}G_5$hex show second-order aggregation of the self-assembled micelles. As more phosphate is bound, the aggregation becomes more pronounced. The concentration of $C_{16}G_5$hex is constant at 1 mM.

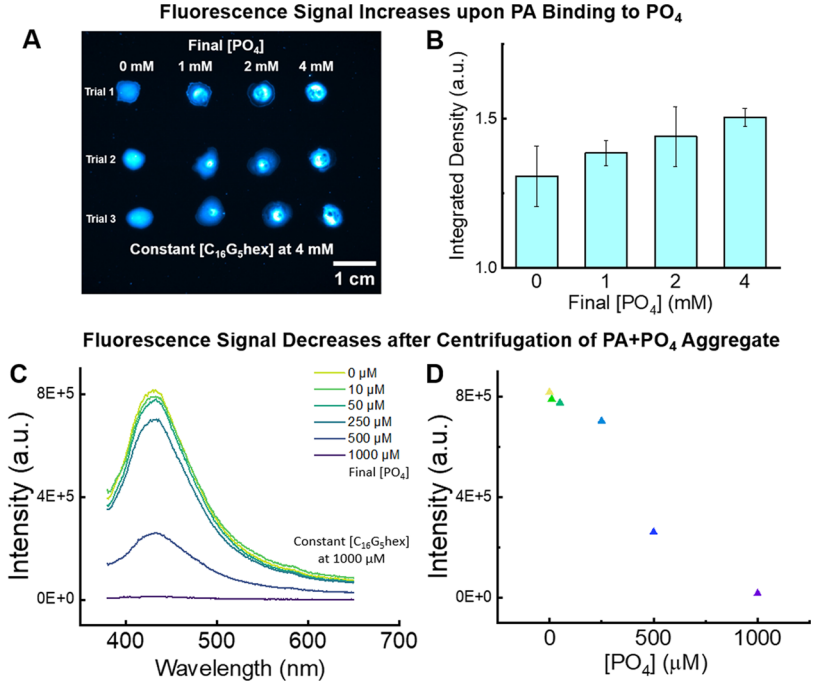

Figure 6. (A) Fluorescence gel microscopy images of 4 mM $C_{16}G_5$hex droplets with increasing final concentration of phosphate, with fluorescence intensity increasing as gelled aggregates form when $C_{16}G_5$hex binds to phosphate. (B) Integrated fluorescence density of the droplet images averaged across three trials quantifies the increase in fluorescence intensity. (C) Emission spectra of the supernatant after centrifugation of 1000 μM $C_{16}G_5$hex with increasing amounts of phosphate. As more phosphate complexes with $C_{16}G_5$hex, the supernatant is depleted of $C_{16}G_5$hex and the emission decreases. (D) Fluorescence intensity of the peak maximums at 430 nm for each phosphate concentration, which linearly decreases as the added phosphate increases.

fully capture phosphate for a recovery application, an optimal sensing material should ideally respond at lower ratios of PA/PO_4 to maximize ligand-to-receptor ratio and increase material efficiency. That ability in $C_{16}G_5$hex is evaluated here. It is also

https://doi.org/10.1021/acs.biomac.2c00960
Biomacromolecules 2022, 23, 4804−4813

interesting to note that self-assembly was found to enhance the binding and selectivity of phosphate in the original study,[7] so this controllable self-assembly now plays a dual role of enhancing binding and triggering intrinsic fluorescence emission.

With the binding ability confirmed, the triggered AIE sensing mechanism was then designed. Several AIE sensing mechanisms have been developed,[53] and the mechanism operating via phase-separation-enhanced emission complements PAMs particularly well. In this mechanism, binding of an AIE material to its target triggers second-order aggregation, likely due to a decrease in solubility of the AIE material upon binding. This phase-separation causes increased emission intensity since the vibrational and rotational motion is decreased for the more tightly packed subfluorophores. Notably, two recent PAMs have reported similar binding-triggered aggregation, including the $C_{16}G_5$hex predecessor. In this previous work, macroscopic aggregates appeared in solution upon binding of phosphate to the PAMs. Another recent PAM was designed by Cui et al. to selectively bind to monoclonal antibodies.[6] Upon binding, the PAMs also phase-separated into a solidlike precipitate, and this was leveraged to extract and purify the target protein.

The second-order aggregation was evaluated and confirmed for $C_{16}G_5$hex. The negative-stain TEM images (Figure 5) visualize the clumping effect at the nanoscale level, with second-order aggregations becoming more pronounced as more phosphate was added. By pairing this inherent aggregation with the newly discovered AIE, $C_{16}G_5$hex is intrinsically positioned to become a highly tunable bioinspired AIE sensing platform.

3.5. Phosphate-Sensing Performance. The preliminary phosphate-sensing characteristics were quantified using gel fluorescence microscopy and fluorometry (Figure 6). The gel fluorescence microscopy images visualized how fluorescence intensity increases as more phosphate is added (Figure 6A), with the phosphate-PA clumps being the more strongly emissive components in the sample droplets. When the ratio of PA/PO_4 is 1:1, the second-order aggregates are noticeably emissive across the three trials. The remaining solution was no longer visibly emissive, with most of the peptide amphiphile likely partitioning into the macroscopic aggregate. The integrated density of the samples in the image were quantified (Figure 6B), confirming that emissive intensities were enhanced when phosphate was added. However, the statistical significance of this method is imprecise, and the sensitivity provided by this technique is limited, with the lowest phosphate concentration tested being 1 mM or 95 ppm. Useful levels of phosphate detection would be in the low ppm range.[53] Thus, this experiment does visualize increased AIE when the material interacts with phosphate, but a more accurate and sensitive method is needed.

To probe the sensitivity limits of this PAM platform, emission studies using a dual-monochromator fluorometer were performed. The samples with the macroscopic aggregates could not be measured with the aggregates *in situ*, since the heterogeneity of the samples produced inconsistent readings. To work around this, the aggregate solutions were centrifuged, and the supernatant containing the unbound PAMs was measured instead. The final $C_{16}G_5$hex concentration of the samples was held constant at 1 mM, and phosphate concentrations ranged from 10 to 1000 μM. The fluorescence of the supernatant was expected to decrease in intensity as more phosphate was added, which would bind to $C_{16}G_5$hex, form an aggregate, and be removed through centrifugation. This effect was observed in the gel fluorescence microscopy images, and it was confirmed in this method in Figure 6C,D.

This method produced more sensitive readings than the gelled image analysis. The peak maxima at 430 nm were plotted versus phosphate concentration in Figure 6D, showing a linear trend that demonstrated binding sensitivity down to 10 μM PO_4 sample. At the other end of the concentration range, a 1:1 ratio of PA/PO_4 showed no fluorescent PA measured in the supernatant, indicating promising molecular sensitivity and efficiency. While future work will optimize the method of measurement to fuse both ease-of-use and sensitivity, overall, this platform is positioned to be competitive with other anion AIE sensors that measure down to the micromolar range and, with optimized design, potentially beyond.

3.6. Discussion Comparing PAMs with Current AIE Materials. It is worthwhile to briefly discuss how PAMs as a new AIE material compare and enhance the robust AIE luminogen (AIEgen) landscape, particularly for biorelated and sensing AIE materials. For a more thorough background, the reader is referred to a recently published review on biomacromolecule AIE platforms, which includes a section on biorelated sensing.[28] A primary difference is the lower QY of these initial PAM systems compared to some other AIE systems, especially those with aromatic components, which can be 10% and higher. The PAM QY of future designs could be enhanced through several means, including increasing the peptide segment length, optimizing the packed state of Region 2, covalently tethering the micelle cores through straightforward click chemistry to reduce molecular motion, or incorporating aromatic amino acids such as tryptophan to enhance AIE. An enhanced QY would make PAMs more readily usable for bioimaging or visualizing targeted drug delivery, and it would likely further enhance the sensitivity for sensing applications.

In terms of advantages, the precise synthetic and structural design control of PAMs is significant. The aforementioned review states, "To date, polymers with precise number of AIEgens are rare··· Development of precise and defined AIE-active biomacromolecules can greatly speed up their biorelated applications."[28] Traditional synthetic approaches add AIEgens as side-chain pendants to polymer backbones, often with a lack of specificity and control.[54] The sequence-specific synthesis of PAMs and their precise tunability to control aggregate structure uniquely sets PAMs apart as an AIE platform.

AIE future directions also largely hinge upon functionalization and stimuli-responsiveness. Other AIE materials have demonstrated stimuli-responsive behavior through unique avenues such as reaction moieties placed in the polymer backbone.[55] PAMs allow for protein-inspired function to be seamlessly incorporated directly into the AIE material, opening up exciting avenues related to many known peptide-targeting moieties. PAMs are also water-soluble highly stable, environmentally benign, and biocompatible, all forward-looking goals for AIEgen development.

4. CONCLUSIONS

In this work, peptide amphiphile micelles, a material platform that has been widely studied and applied for more than two decades, were discovered to be a new AIE material that features precise synthetic control, self-assembling tunability, and bioinspired functionality. The absorbance, excitation, and emission properties were consistent with previously identified AIE systems that utilize amides as the emission pathways. The

https://doi.org/10.1021/acs.biomac.2c00960
Biomacromolecules 2022, 23, 4804−4813

fluorescence critical micelle concentration was found to be ~1.5 orders of magnitude higher than the true critical micelle concentration, suggesting that a critical number of PAs must be assembled into the micelle to display AIE. $C_{16}G_5$hex had the highest quantum yield of the three peptide amphiphile micelles tested, which was attributed to the random coil arrangement of the peptide chains in the micelle corona and the increased number of emission pathways due to a higher number of amino acid residues being present. This direct impact of tuning molecular factors to impact AIE presents peptide amphiphile micelles as a highly engineerable AIEgen. $C_{16}G_5$hex was then evaluated as a phosphate-sensing AIE material by harnessing a protein-extracted binding sequence, and it was able to detect phosphate by utilizing a second-order aggregation stimulus down to a sensitivity of 1 ppm phosphate. Overall, peptide amphiphile micelles demonstrate that pairing synthetic protein mimicry with intrinsic AIE fluorescence opens up a wide array of new AIE applications for this already well-characterized and highly tunable material.

■ ASSOCIATED CONTENT

Supporting Information

The Supporting Information is available free of charge at https://pubs.acs.org/doi/10.1021/acs.biomac.2c00960.

Additional data including LC−MS purity and mass spectra; absorption, excitation, emission, and CMC data for $C_{16}G_5$K and $C_{16}S_5$hex; quantum yield calculations; TEM; CD spectra with fitted curves; and verification of selective binding of $C_{16}G_5$hex (PDF)

A three-dimensional (3D) rendering of the micelles suspended in the droplet using confocal fluorescence microscopy (Video S1) (AVI)

■ AUTHOR INFORMATION

Corresponding Author

Whitney C. Fowler − *Department of Engineering, Harvey Mudd College, Claremont, California 91711, United States;* orcid.org/0000-0002-8088-4744; Email: wfowler@g.hmc.edu

Complete contact information is available at: https://pubs.acs.org/10.1021/acs.biomac.2c00960

Notes

The author declares no competing financial interest.

■ ACKNOWLEDGMENTS

W.C.F. acknowledges support from the National Science Foundation (NSF) under the Graduate Research Fellowship Program Grant No. DGE-1746045 and the Division of Materials Research Grant No. DMR-2119681. This work was conducted in the Pritzker School of Molecular Engineering at the University of Chicago as part of its Materials for Sustainability Theme. The author acknowledges the University of Chicago's Advanced Electron Microscopy Core Facility for acquiring the TEM images, the University of Chicago's Integrated Light Microscopy Core Facility for assistance with acquiring the confocal fluorescence microscopy images, the University of Chicago Biophysics Core facility where the fluorometer data and gel imager data were acquired, the University of Chicago Soft Matter Characterization facility where the UV−vis Absorbance data were acquired, and the University of Chicago's Mass Spectroscopy Core Facility, where LC−MS data were acquired. Analyte analysis by ion chromatography was performed at the Northwestern University Quantitative Bio-element Imaging Center. The author thanks Matthew Tirrell who provided advice and encouragement during this work.

■ REFERENCES

(1) Berndt, P.; Fields, G. B.; Tirrell, M. Synthetic Lipidation of Peptides and Amino Acids: Monolayer Structure and Properties. *J. Am. Chem. Soc.* **1995**, *117*, 9515−9522.

(2) Yu, Y. C.; Berndt, P.; Tirrell, M.; Fields, G. B. Self-Assembling Amphiphiles for Construction of Protein Molecular Architecture. *J. Am. Chem. Soc.* **1996**, *118*, 12515−12520.

(3) Hartgerink, J. D.; Beniash, E.; Stupp, S. I. Self-Assembly and Mineralization of Peptide-Amphiphile Nanofibers. *Science* **2001**, *294*, 1684−1688.

(4) Hendricks, M. P.; Sato, K.; Palmer, L. C.; Stupp, S. I. Supramolecular Assembly of Peptide Amphiphiles. *Acc. Chem. Res.* **2017**, *50*, 2440−2448.

(5) Acar, H.; Samaeekia, R.; Schnorenberg, M. R.; Sasmal, D. K.; Huang, J.; Tirrell, M. V.; LaBelle, J. L. Cathepsin-Mediated Cleavage of Peptides from Peptide Amphiphiles Leads to Enhanced Intracellular Peptide Accumulation. *Bioconjugate Chem.* **2017**, *28*, 2316−2326.

(6) Li, Y.; Lock, L. L.; Mills, J.; Ou, B. S.; Morrow, M.; Stern, D.; Wang, H.; Anderson, C. F.; Xu, X.; Ghose, S.; Li, Z. J.; Cui, H. Selective Capture and Recovery of Monoclonal Antibodies by Self-Assembling Supramolecular Polymers of High Affinity for Protein Binding. *Nano Lett.* **2020**, *20*, 6957−6965.

(7) Fowler, W. C.; Deng, C.; Gri, G. M.; Teodoro, T.; Guo, A. Z.; Zaiden, M.; Gottlieb, M.; Pablo, J. J.; De; Tirrell, M. V. Harnessing Peptide Binding to Capture and Reclaim Phosphate. *J. Am. Chem. Soc.* **2021**, *143*, 4440−4450.

(8) Black, K. A.; Lin, B. F.; Wonder, E. A.; Desai, S. S.; Chung, E. J.; Ulery, B. D.; Katari, R. S.; Tirrell, M. V. Biocompatibility and Characterization of a Peptide Amphiphile Hydrogel for Applications in Peripheral Nerve Regeneration. *Tissue Eng., Part A* **2015**, *21*, 1333−1342.

(9) Álvarez, Z.; Kolberg-Edelbrock, A. N.; Sasselli, I. R.; Ortega, J. A.; Qiu, R.; Syrgiannis, Z.; Mirau, P. A.; Chen, F.; Chin, S. M.; Weigand, S.; Kiskinis, E.; Stupp, S. I. Bioactive Scaffolds with Enhanced Supramolecular Motion Promote Recovery from Spinal Cord Injury. *Science* **2021**, *374*, 848−856.

(10) Trent, A.; Marullo, R.; Lin, B.; Black, M.; Tirrell, M. Structural Properties of Soluble Peptide Amphiphile Micelles. *Soft Matter* **2011**, *7*, 9572−9582.

(11) Greenfield, M. A.; Hoffman, J. R.; De La Cruz, M. O.; Stupp, S. I. Tunable Mechanics of Peptide Nanofiber Gels. *Langmuir* **2010**, *26*, 3641−3647.

(12) Kastantin, M.; Missirlis, D.; Ananthanarayanan, B.; Neumann, T.; Tirrell, M.; Farine, M. Linker Chemistry Determines Secondary Structure of P53 14−29 in Peptide Amphiphile Micelles. *Bioconjugate Chem.* **2010**, *21*, 465−475.

(13) Missirlis, D.; Chworos, A.; Fu, C. J.; Khant, H. A.; Krogstad, D. V.; Tirrell, M. Effect of the Peptide Secondary Structure on the Peptide Amphiphile Supramolecular Structure and Interactions. *Langmuir* **2011**, *27*, 6163−6170.

(14) Barrett, J. C.; Ulery, B. D.; Trent, A.; Liang, S.; David, N. A.; Tirrell, M. V. Modular Peptide Amphiphile Micelles Improving an Antibody-Mediated Immune Response to Group A Streptococcus. *ACS Biomater. Sci. Eng.* **2017**, *3*, 144−152.

(15) Behanna, H. A.; Donners, J. J. J. M.; Gordon, A. C.; Stupp, S. I. Coassembly of Amphiphiles with Opposite Peptide Polarities into Nanofibers. *J. Am. Chem. Soc.* **2005**, *127*, 1193−1200.

(16) Ye, R.; Liu, Y.; Zhang, H.; Su, H.; Zhang, Y.; Xu, L.; Hu, R.; Kwok, R. T. K.; Wong, K. S.; Lam, J. W. Y.; Goddard, W. A.; Tang, B. Z. Non-Conventional Fluorescent Biogenic and Synthetic Polymers without Aromatic Rings. *Polym. Chem.* **2017**, *8*, 1722−1727.

(17) Chatterjee, D. P.; Pakhira, M.; Nandi, A. K. Fluorescence in "Nonfluorescent" Polymers. *ACS Omega* **2020**, *5*, 30747−30766.

(18) Wang, Y.; Bin, X.; Chen, X.; Zheng, S.; Zhang, Y.; Yuan, W. Z. Emission and Emissive Mechanism of Nonaromatic Oxygen Clusters. *Macromol. Rapid Commun.* **2018**, *39*, 1−6.
(19) Gong, Y.; YeQiang, T.; Ju, M.; Yiren, Z.; WangZhang, Y.; YongMing, Z.; JingZhi, S.; Zhong, T. B. Room Temperature Phosphorescence from Natural Products: Crystallization Matters. *Sci. China: Chem.* **2013**, *56*, 1178−1182.
(20) Niu, S.; Yan, H.; Chen, Z.; Li, S.; Xu, P.; Zhi, X. Unanticipated Bright Blue Fluorescence Produced from Novel Hyperbranched Polysiloxanes Carrying Unconjugated Carbon-Carbon Double Bonds and Hydroxyl Groups. *Polym. Chem.* **2016**, *7*, 3747−3755.
(21) Liu, C.; Cui, Q.; Wang, J.; Liu, Y.; Chen, J. Autofluorescent Micelles Self-Assembled from an AIE-Active Luminogen Containing an Intrinsic Unconventional Fluorophore. *Soft Matter* **2016**, *12*, 4295−4299.
(22) Homchaudhuri, L.; Swaminathan, R. Novel Absorption and Fluorescence Characteristics of L-Lysine. *Chem. Lett.* **2001**, *30*, 844−845.
(23) Homchaudhuri, L.; Swaminathan, R. Near Ultraviolet Absorption Arising from Lysine Residues in Close Proximity: A Probe to Monitor Protein Unfolding and Aggregation in Lysine-Rich Proteins. *Bull. Chem. Soc. Jpn.* **2004**, *77*, 765−769.
(24) Luo, J.; Xie, Z.; Xie, Z.; Lam, J. W. Y.; Cheng, L.; Chen, H.; Qiu, C.; Kwok, H. S.; Zhan, X.; Liu, Y.; Zhu, D.; Tang, B. Z. Aggregation-Induced Emission of 1-Methyl-1,2,3,4,5-Pentaphenylsilole. *Chem. Commun.* **2001**, *18*, 1740−1741.
(25) del Marcato, L. L.; Pompa, P. P.; Maruccio, G.; Torre, A. D.; Sabella, S.; Tamburro, A. M.; Cingolani, R.; Rinaldi, R. Correction for Del Mercato et al., Charge Transport and Intrinsic Fluorescence in Amyloid-like Fibrils. *Proc. Natl. Acad. Sci.* **2008**, *105*, 6208.
(26) Yu, Y.; Gim, S.; Kim, D.; Arnon, Z. A.; Gazit, E.; Seeberger, P. H.; Delbianco, M. Oligosaccharides Self-Assemble and Show Intrinsic Optical Properties. *J. Am. Chem. Soc.* **2019**, *141*, 4833−4838.
(27) Chen, X.; Luo, W.; Ma, H.; Peng, Q.; Yuan, W. Z.; Zhang, Y. Prevalent Intrinsic Emission from Nonaromatic Amino Acids and Poly(Amino Acids). *Sci. China: Chem.* **2018**, *61*, 351−359.
(28) Hu, R.; Wang, J.; Qin, A.; Tang, B. Z. Aggregation-Induced Emission-Active Biomacromolecules: Progress, Challenges, and Opportunities. *Biomacromolecules* **2022**, *23*, 2185−2196.
(29) Kang, M.; Zhang, Z.; Song, N.; Li, M.; Sun, P.; Chen, X.; Wang, D.; Tang, B. Z. Aggregation-enhanced Theranostics: AIE Sparkles in Biomedical Field. *Aggregate* **2020**, *1*, 80−106.
(30) Huang, X.; Gu, X.; Zhang, G.; Zhang, D. A Highly Selective Fluorescence Turn-on Detection of Cyanide Based on the Aggregation of Tetraphenylethylene Molecules Induced by Chemical Reaction. *Chem. Commun.* **2012**, *48*, 12195−12197.
(31) Neupane, L. N.; Oh, E. T.; Park, H. J.; Lee, K. H. Selective and Sensitive Detection of Heavy Metal Ions in 100% Aqueous Solution and Cells with a Fluorescence Chemosensor Based on Peptide Using Aggregation-Induced Emission. *Anal. Chem.* **2016**, *88*, 3333−3340.
(32) Gao, M.; Tang, B. Z. Fluorescent Sensors Based on Aggregation-Induced Emission: Recent Advances and Perspectives. *ACS Sens.* **2017**, *2*, 1382−1399.
(33) Bao, P.; Li, C.; Ou, H.; Ji, S.; Chen, Y.; Gao, J.; Yue, X.; Shen, J.; Ding, D. A Peptide-Based Aggregation-Induced Emission Bioprobe for Selective Detection and Photodynamic Killing of Gram-Negative Bacteria. *Biomater. Sci.* **2021**, *9*, 437−442.
(34) Wu, T.; Huang, J.; Yan, Y. Self-Assembly of Aggregation-Induced-Emission Molecules. *Chem. - Asian J.* **2019**, *14*, 730−750.
(35) Sivaguru, M.; Khaw, Y. M.; Inoue, M. A Confocal Reflection Super-Resolution Technique to Image Golgi-Cox Stained Neurons. *J. Microsc.* **2019**, *275*, 115−130.
(36) Tu, R. S.; Tirrell, M. Bottom-up Design of Biomimetic Assemblies. *Adv. Drug Delivery Rev.* **2004**, *56*, 1537−1563.
(37) Cui, H.; Webber, M. J.; Stupp, S. I. Self-Assembly of Peptide Amphiphiles: From Molecules to Nanostructures to Biomaterials. *Pept. Sci.* **2010**, *94*, 1−18.
(38) Saraste, M.; Sibbald, P. R.; Wittinghofer, A. The P-Loop-a Common Motif in ATP- and GTP-Binding Proteins. *Trends Biochem. Sci.* **1990**, *15*, 430−434.
(39) Paramonov, S. E.; Jun, H. W.; Hartgerink, J. D. Self-Assembly of Peptide-Amphiphile Nanofibers: The Roles of Hydrogen Bonding and Amphiphilic Packing. *J. Am. Chem. Soc.* **2006**, *128*, 7291−7298.
(40) Lin, L. Y.; Huang, P. C.; Yang, D. J.; Gao, J. Y.; Hong, J. L. Influence of the Secondary Structure on the AIE-Related Emission Behavior of an Amphiphilic Polypeptide Containing a Hydrophobic Fluorescent Terminal and Hydrophilic Pendant Groups. *Polym. Chem.* **2016**, *7*, 153−163.
(41) Li, S. T.; Lin, Y. C.; Kuo, S. W.; Chuang, W. T.; Hong, J. L. Aggregation Induced Emission Enhancement in Relation to the Secondary Structures of Poly(γ-Benzyl-l-Glutamate) Containing a Fluorescent Tetraphenylthiophene Moiety. *Polym. Chem.* **2012**, *3*, 2393−2402.
(42) Israelachvili, J. N.; Mitchell, D. J.; Ninham, B. W. Theory of Self-Assembly of Hydrocarbon Amphiphiles into Micelles and Bilayers. *J. Chem. Soc., Faraday Trans. 2* **1976**, *72*, 1525.
(43) Stuart, M. C. A.; Boekema, E. J. Two Distinct Mechanisms of Vesicle-to-Micelle and Micelle-to-Vesicle Transition Are Mediated by the Packing Parameter of Phospholipid−Detergent Systems. *Biochim. Biophys. Acta, Biomembr.* **2007**, *1768*, 2681−2689.
(44) Ghosh, A.; Haverick, M.; Stump, K.; Yang, X.; Tweedle, M. F.; Goldberger, J. E. Fine-Tuning the PH Trigger of Self-Assembly. *J. Am. Chem. Soc.* **2012**, *134*, 3647−3650.
(45) Zhang, X.; Jackson, J. K.; Burt, H. M. Determination of Surfactant Critical Micelle Concentration by a Novel Fluorescence Depolarization Technique. *J. Biochem. Biophys. Methods* **1996**, *31*, 145−150.
(46) Melhuish, W. H. Quantum Efficiencies of Fluorescence of Organic Substances: Effect of Solvent and Concentration of the Fluorescent Solute. *J. Phys. Chem. A* **1961**, *65*, 229−235.
(47) Zhang, Z.; Xiong, J.; He, G.; Dang, D.; Xie, Y.; Wang, Q. Fluorous Effect-Induced Emission of Azido Substituted Poly(Vinylidene Fluoride) with High Photostability and Film Formation. *Polym. Chem.* **2020**, *11*, 1307−1313.
(48) Marullo, R.; Kastantin, M.; Drews, L. B.; Tirrell, M. Peptide Contour Length Determines Equilibrium Secondary Structure in Protein-Analogous Micelles. *Biopolymers* **2013**, *99*, 573−581.
(49) Smith, V. H.; Schindler, D. W. Eutrophication Science: Where Do We Go from Here? *Trends Ecol. Evol.* **2009**, *24*, 201−207.
(50) Cordell, D.; Rosemarin, A.; Schröder, J. J.; Smit, A. L. Towards Global Phosphorus Security: A Systems Framework for Phosphorus Recovery and Reuse Options. *Chemosphere* **2011**, *84*, 747−758.
(51) Desmidt, E.; Ghyselbrecht, K.; Zhang, Y.; Pinoy, L.; Van Der Bruggen, B.; Verstraete, W.; Rabaey, K.; Meesschaert, B. Global Phosphorus Scarcity and Full-Scale P-Recovery Techniques: A Review. *Crit. Rev. Environ. Sci. Technol.* **2015**, *45*, 336−384.
(52) Mapare, S. V.; Yu, P.-L.; Sarkar, A.; Mukhopadhyay, S. C. In *A Review of Sensor Technology for In-Field Phosphate Monitoring*, Seventh International Conference on Sensing Technology (ICST); IEEE, 2013; pp 411−418.
(53) Chua, M. H.; Shah, K. W.; Zhou, H.; Xu, J. Recent Advances in Aggregation-Induced Emission Chemosensors for Anion Sensing. *Molecules* **2019**, *24*, 1−42.
(54) Chen, J.; Xie, Z.; Lam, J. W. Y.; Law, C. C. W.; Tang, B. Z. Silole-Containing Polyacetylenes. Synthesis, Thermal Stability, Light Emission, Nanodimensional Aggregation, and Restricted Intramolecular Rotation. *Macromolecules* **2003**, *36*, 1108−1117.
(55) Sun, Y.; Neary, W. J.; Burke, Z. P.; Qian, H.; Zhu, L.; Moore, J. S. Mechanically Triggered Carbon Monoxide Release with Turn-On Aggregation-Induced Emission. *J. Am. Chem. Soc.* **2022**, *144*, 1125−1129.

https://doi.org/10.1021/acs.biomac.2c00960
Biomacromolecules 2022, 23, 4804−4813